Journal of Physics D: Applied Physics

PURPOSE-LED PUBLISHING™

PAPER • **OPEN ACCESS**

Terahertz phase imaging of large-aperture liquid crystal modulator with ITO interdigitated electrode

To cite this article: A Le Bourlout *et al* 2024 *J. Phys. D: Appl. Phys.* **57** 505101

OPEN ACCESS
IOP Publishing
Journal of Physics D: Applied Physics
J. Phys. D: Appl. Phys. **57** (2024) 505101 (8pp)
https://doi.org/10.1088/1361-6463/ad7a87

Terahertz phase imaging of large-aperture liquid crystal modulator with ITO interdigitated electrode

A Le Bourlout[1], A Pusenkova[2], J Lafrenière-Greig[1], X Ropagnol[1,3], T Galstian[2] and F Blanchard[1,*]

[1] Department of Electrical Engineering, École de Technologie Supérieure, Montréal, Québec, Canada
[2] Département de Génie Physique, Université de Laval (ULaval), Québec, Canada
[3] Institut National de la Recherche Scientifique—Énergie Matériaux Télécommunications, Varennes, Québec, Canada

E-mail: francois.blanchard@etsmtl.ca

Received 18 July 2024, revised 6 September 2024
Accepted for publication 12 September 2024
Published 20 September 2024

Abstract

We have fabricated and characterized a large-aperture electrooptic phase modulation device operating in the terahertz (THz) frequency range. The device consists of a 1.6 mm thick nematic liquid crystal placed between glass plates with a novel interdigitated electrode design. Using THz time-domain spectroscopy (THz-TDS) coupled with raster scanning imaging, we evaluated phase modulation across a 25 mm diameter LC device and mapped the spatial uniformity of phase shift. Our results confirm the functionality of the LC cell as a controllable quarter-wave plate at 0.26 THz and half-wave plate at 0.52 THz. This work contributes to the development of large-aperture and transmissive LC devices as low-cost phase plates for THz waves and paves the way for future applications in THz modulators.

Keywords: terahertz, liquid crystal, time-domain spectroscopy, phase plate

1. Introduction

Terahertz (THz) modulators are key components for several emerging applications, notably in communications [1] and imaging [2]. In both fields, filtering and active control of amplitude, phase and frequency are highly desirable, for example in the development of reconfigurable intelligent surfaces (RISs) [3]. Since these waves are naturally larger than those of the visible (VIS) or near infrared (NIR) wavelengths, they offer certain advantages while posing other challenges. For example, they promise to make THz filters or resonant structure easier to manufacture, without the need for complex cleanroom techniques [4]. For active control, liquid crystal (LC), sometime coupled with a resonant structure, remain a particularly attractive choice [5]. As with VIS light applications [6, 7], the anisotropic and dielectric properties of LCs could significantly expand the range of THz applications, enabling cutting-edge technologies such as phase shifters [8–10], absorbers and filters [11–13], RIS with delay lines [14], and frequency shifters [15–17], among others. For instance, in these demonstrations, most designs incorporate a resonant structure in combination with an LC material (metadevices). In this way, the resonant structure effectively captures THz waves at the operating frequency, while minimizing the interaction length with the LC material.

Surprizingly enough, some of these LC materials may have rather significant (at the order of 0.2–0.3) birefringence $\Delta n = n_{\parallel} - n_{\perp}$ at THz frequencies, where $n_{\parallel}$ and $n_{\perp}$ are, respectively, refractive index values for the electric displacement vector that is parallel and perpendicular to the direction of natural alignment of long molecular axes of the LC, often called director

* Author to whom any correspondence should be addressed.

[18]. In addition, the dielectric torque, applied by rather moderate voltages (few volts) may reorient the director, changing thus the optical path difference (OPD), from PD $=n_{\parallel}d$ to $n_{\perp}d$, where d is the thickness of the LC, providing thus a maximal possible change of OPD $=\Delta nd$. However, there are important differences compared with VIS or NIR ranges. THz waves are generally collimated using large optics, such as parabolic mirrors 25–50 mm in diameter. Consequently, THz modulators and filters of similar size are needed to achieve modulation in the flat phase distribution plane, i.e. not at the focus. In addition, the use of broadband pulses in trasnmission mode may prove difficult if the modulator consists of an LC metadevice. Despite a notable increase in interest in various types of modulators in current scientific research [1, 19], there has been only limited investigation into large-aperture and broadband LC modulators operating in the THz range [20, 21].

Achieving this goal requires further exploration of two primary factors: (i) integrating electrode configurations that minimally interact with THz waves [22, 23], and (ii) understanding the relationship between the long interaction length of THz waves with LCs and their high absorption in liquids [24]. Indeed, it is worth mentioning that, in the transmission mode (which is our main interest), larger is the sample, further away the peripheral metal electrodes must be placed to drive the LC, which inevitably will increase the required voltages [21]. Alternative approaches were explored, for example, by using carbon nano tube surfaces [23]. However, the industrial process for manufacturing thin films of these materials is not yet well established. In addition, the two-dimensional (2D) uniformity of LCs in cells with layers a millimeter thick or more—essential for inducing significant birefringence in the THz range—has not been confirmed. Successful manufacture and characterization of these large LC cells could pave the way for new phase plates of various shapes, such as vector beams [25], tailored to the desired operating frequency. It is therefore essential to develop and demonstrate multiple alternatives for broadband, low-loss, large-aperture active LC devices operating in the THz range.

In this work, we present a new large-aperture LC cell structure featuring interdigitated electrodes with low losses for THz waves. The cell features a 25 mm diameter aperture operating in the 0–1 THz range. To characterize the LC sample with its new electrode design, we used THz time-domain spectroscopy (THz-TDS). Unlike optical measurements, which rely on sensors to obtain intensity, the time-resolved capability of THz-TDS allows us to capture both the amplitude and phase of the electric field [26]. This feature makes THz-TDS particularly useful for characterizing phase modulators such as LC devices. Combined with a raster scanning unit, it provides a complete 2D mapping of the uniformity of LC devices. In addition to the spatial distribution of cell birefringence, our results show a significant phase shift of 7 rad THz^{-1}. We have also confirmed the minimal losses associated with the thin indium tin oxide (ITO) interdigital electrode when oriented in the optimum operating position. Finally, real-time measurements of the device at 300 GHz reveal a switching time of 16 s followed by a slow natural reorientation of almost an hour after the bias voltage (V-bias) is switched off.

2. Materials and methods

2.1. LC sample

We have used here a nematic LC, which is an anisotropic fluid [18] with an anisotropy axis (along the unit vector n, called director; and defined by the average molecular orientation of the LC) that can be reoriented by external electric or magnetic fields [21, 22]. This allows the dynamic manipulation of the effective extraordinary refractive index n_e of the LC:

$$n_e(\theta) = \frac{n_{\parallel}n_{\perp}}{\sqrt{n_{\perp}^2\sin^2\theta + n_{\parallel}^2\cos^2\theta}}, \tag{1}$$

where θ is the angle between the wavevector and the director; $n_{\parallel}$ and $n_{\perp}$ are refractive index values for electric inductions aligned, respectively, along the director and in the perpendicular direction. The value $\Delta n = n_{\parallel} - n_{\perp}$ is defined as optical birefringence of the medium.

Novel compounds have been synthesized to increase the birefringence and reduce absorption and dichroism in microwave and THz ranges [24]. The value of birefringence is crucial for THz phase shifters, as it dictates the amount of liquid required for the desired function. The maximal achievable optical phase difference $\Delta\varphi$ can be estimated using the following equation:

$$\Delta\varphi = \Delta nd\frac{2\pi}{\lambda_0}, \tag{2}$$

where λ_0 is the wavelength in vacuum.

Typically, the VIS applications (e.g. $\lambda_0 = 0.5$ μm) require LC cells of micrometer thicknesses. However, in the THz domain (with wavelengths at the order of 1 mm) they must be much thicker (in the order of millimeters) to reach noticeable phase modulations. This makes the reorientation times longer (minutes) [14] and create challenges in the cell orientation and tunability.

The sample, illustrated in figure 1(a), contains LCs that are 1600 μm thick with a clear aperture diameter of 1 inch (25 mm). It is filled with mixture 1825 of nematic LC, whose properties are described in detail in [24]. This cell consists of two glass substrates with a thickness $t = 550$ μm. A thin layer (40 nm) of polyimide is applied, baked, and rubbed to maintain the planar orientation of the LC molecules. The glass substrates are bonded together using UV glue, with LC filled in between.

Generally, for applications with electromagnetic waves located in the VIS spectrum, electrodes are made from a homogenous thin layer of conductive ITO, directly deposited onto the substrates. This is already a very well-established technology in the display industry, which explains our interest to these materials. However, ITO film is only transparent in the VIS and near-IR range, while completely attenuating

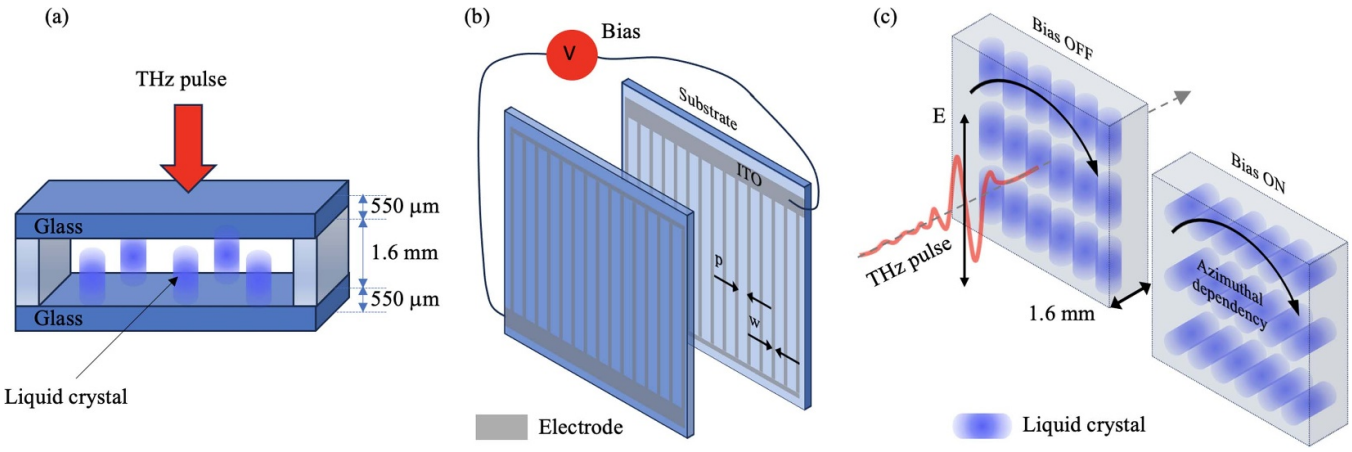

Figure 1. (a) Illustration of the LC sample with its physical dimension. (b) Configuration of the electrodes deposited on the glass substrate. p: pitch and w: lane width. The liquid crystal is inserted between the two substrates. (c) Illustration of molecule orientation as a function of bias voltage.

THz waves. This approach is therefore unsuitable for THz applications, and another electrode solution needs to be proposed, such as, side electrodes [27]. The present paper proposes an interdigital ITO electrode design (see figure 1(b)), composed of thin patterned ITO tracks of about 30 nm width, with a periodicity (pitch) of 370 μm [28]. This structure is similar to metal-grid THz polarizers, which are commonly used to polarize or attenuate THz waves [29]. Our experiments with linearly polarized THz pulses show that this specific patterned ITO configuration achieves near-perfect transmission in the operating orientation. In addition, the use of a LC layer thicker than 1 mm allows relatively large interdigitated electrode spacings (370 μm), as the electric field inside the LC layer is smoothed [21]. This approach is particularly promising for transmission-mode phase modulation applications.

Figure 1(c) shows the two experimental conditions, i.e. with and without the application of a V-bias, and illustrates the orientation of LC molecules' as a function of V-bias. To induce a phase shift on the THz wave, a square voltage of 1 kHz and 20 volts AC was applied to the electrodes. Initially, with no voltage applied, the LC molecules align parallel to the cell substrates and along the direction perpendicular of the electrode's stripes. Upon applying voltage, molecules align along the bias field direction. This direction is parallel to the THz beam propagation. Therefore, when the biased voltage is applied, no change in refractive index is expected with respect to the rotation angle of the LC cell (i.e. no perceived birefringence exists). We therefore study the THz properties of our LC cell by measuring the THz pulses transmitted at 10° angular intervals, from 0° to 360°, when the voltage is switched off, then repeating this measurement when the voltage is switched on. To validate the phase change obtained when the electric field is applied, we calculate the differential between the phase values for the voltage-on and voltage-off measurements for each angle of rotation. It should be noted that our measurements were carried out over the entire aperture using a 2D time-domain scan. It is important to note that a THz polarizer is placed before the LC cell to ensure that only linearly polarized light passes through the sample.

2.2. *Experimental setup TDS*

Figure 2(a) shows the THz-TDS used in this experiment, a Toptica system, model TeraFlash pro, which uses InGaAs photoconductive antennas for emission and detection, pumped by laser pulses with a wavelength of 1550 nm. As this figure also shows, THz radiation is collected and guided by four one-inch diameter 90° off-axis parabolic mirrors (OAPMs). The sample is placed at the focal point of the THz beam, between the second and third OAPMs. A 2-inch-diameter wire-grid polarizer is placed before the sample to ensure that the incoming THz beam is linearly polarized. The TeraFlash system allows spectroscopic measurements from 100 GHz to 4 THz, as shown in figure 2(b) with the time-domain traces in inset. However, due to the absorption in the two glass substrates, measurements are limited to the 100–1000 GHz range. The measurement of the reference pulse was done in ambient air.

To understand the impact of the electrodes, substrates, and LCs, we examine THz pulses through three configurations: (1) a single glass substrate plate, (2) a glass plate with an ITO interdigital electrode, and (3) a complete cell with two substrates and electrodes but without LC material. Notably in figure 2(b), the spectrum of the substrate (yellow) completely overlaps with that of the configuration with one electrode when the latter is set perpendicular to the THz field polarization [29]. Additionally, the spectra of the empty cell (green) and the cell containing LCs (red) are mostly equivalent, as expected given that the absorption of the LC mixture is about 5 cm^{-1} in this frequency range [24]. Using these data and equation (5) as presented in the next section, we determined that the extraordinary index at 300 GHz was 1.76 for the LC used in this study. This value was obtained by analyzing the time-domain traces of the cell containing the LC and the cell without the LC.

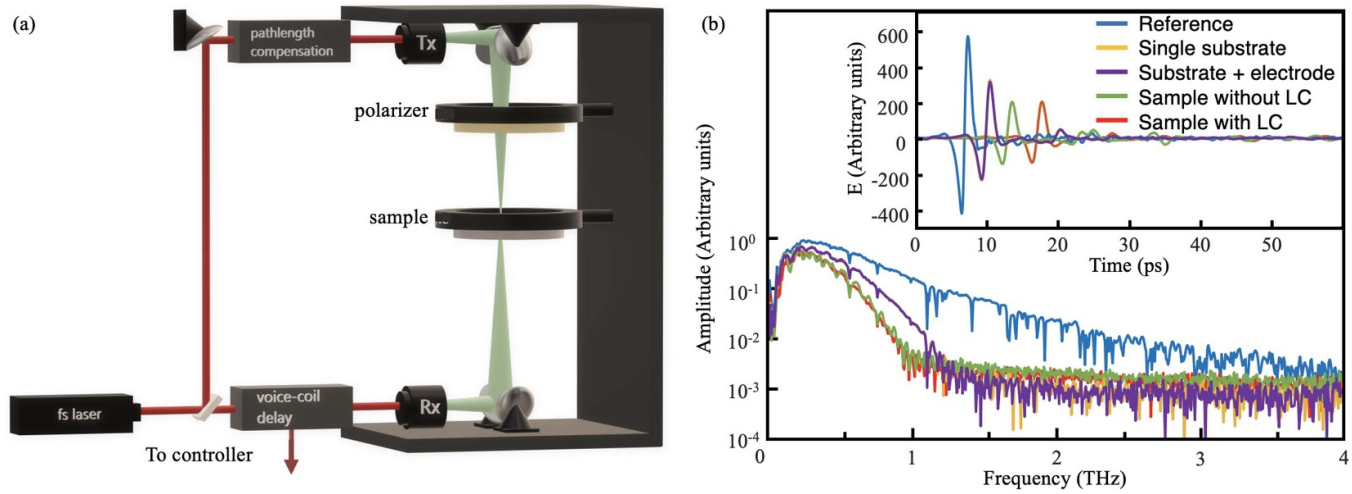

Figure 2. (a) Schematic of the THz-TDS system. (b) Spectra of Fourier transform of the THz pulse and the time-domain signal in inset of the reference (blue) and the various sample components.

As we will discuss below, the phase needs some extra care to have a good correlation between biased and unbiased measurement. Moreover, this situation becomes more critical if 2D mapping is performed [2, 30]. Indeed, it should be noted that the LC assessment, carried out in this work, was obtained by systematically scanning the entire LC cell via a raster scanning. The imaging device comprises two precise linear stages for scanning the sample through the focus of the THz beam. For this sample, the imaging area covers 25 $\times$ 25 mm^2 with a resolution of 0.5 mm in each axis, resulting in a total of 2500 THz traces. To better understand the transmission behavior and phase change of the LC device, we will also present the azimuthal dependence of the normalized amplitude and phase information in the next section.

3. Results and discussion

3.1. Normalized transmission

Unlike the complexity of active phase-change measurements in reflection mode [30], THz measurements in transmission mode are easier to perform because the path, travelled by the THz beam, remains constant between measurements. However, significant absorption in samples can introduce a substantial error in phase change, particularly when the phase starts to wrap around itself. In transmission, the sample is mounted at normal incidence with respect to the propagation direction of the THz radiation. This prevents additional signal losses caused by lateral shift of the THz beam, which occurs due to refraction in the sample. The measured transmission function of a sample and a reference measurement can be express as follow [26]:

$$\widetilde{T}(f) = \frac{\widetilde{E}_s(f)}{\widetilde{E}_r(f)} = |T|\, e^{i\Delta\phi} \tag{3}$$

where $\tilde{E}_s(f)$ is the Fourier-transformed time trace recorded through the sample, $\tilde{E}_r(f)$ is the Fourier-transformed reference time trace recorded through air, $|T|$ is the transmission amplitude and $\Delta\phi$ is the frequency-resolved phase difference between the two signals.

Measurement of phase and spectral amplitude enables direct calculation of complex-valued physical properties of materials, such as absorption α and refractive index n. The equations used for these calculations are well-known and provided below [26]:

$$\alpha(f) = -\frac{2}{d}\ln\left[|T|\frac{(n+1)^2}{4n}\right], \tag{4}$$

$$n(f) = 1 + \frac{c\Delta\phi}{2\pi f d} \tag{5}$$

where c is the speed of light and f is the THz frequency

The initial evaluation of the LC device aims to understand the influence of the electrodes and polarization field on THz wave transmission as a function of cell rotation, i.e. keeping the incoming THz polarization fixed. Indeed, significant transmission losses from the electrodes would render it ineffective as an active phase modulator. It is therefore important to determine if the electrode is properly aligned with the operating orientation angle of the LC device. Figure 3(a) shows a VIS image of the LC device used for analyzing transmission as a function of rotation. Figure 3(b) shows the variation in phase ($\Delta\Phi$) or normalized phase, obtained by subtracting the phase information under bias-off conditions from that under bias-on conditions. This figure shows two distinct regions: one with strong phase changes and the other with no phase change. This behavior is repeated twice over the entire rotation, as expected due to the symmetry of the elongation shape of the LC. In this figure, we will focus our analysis on two specific angles, as indicated by the two orange dotted lines: 270 degrees for significant phase modulation and 180 degrees for a region with no phase change. The extraction of the phase difference for

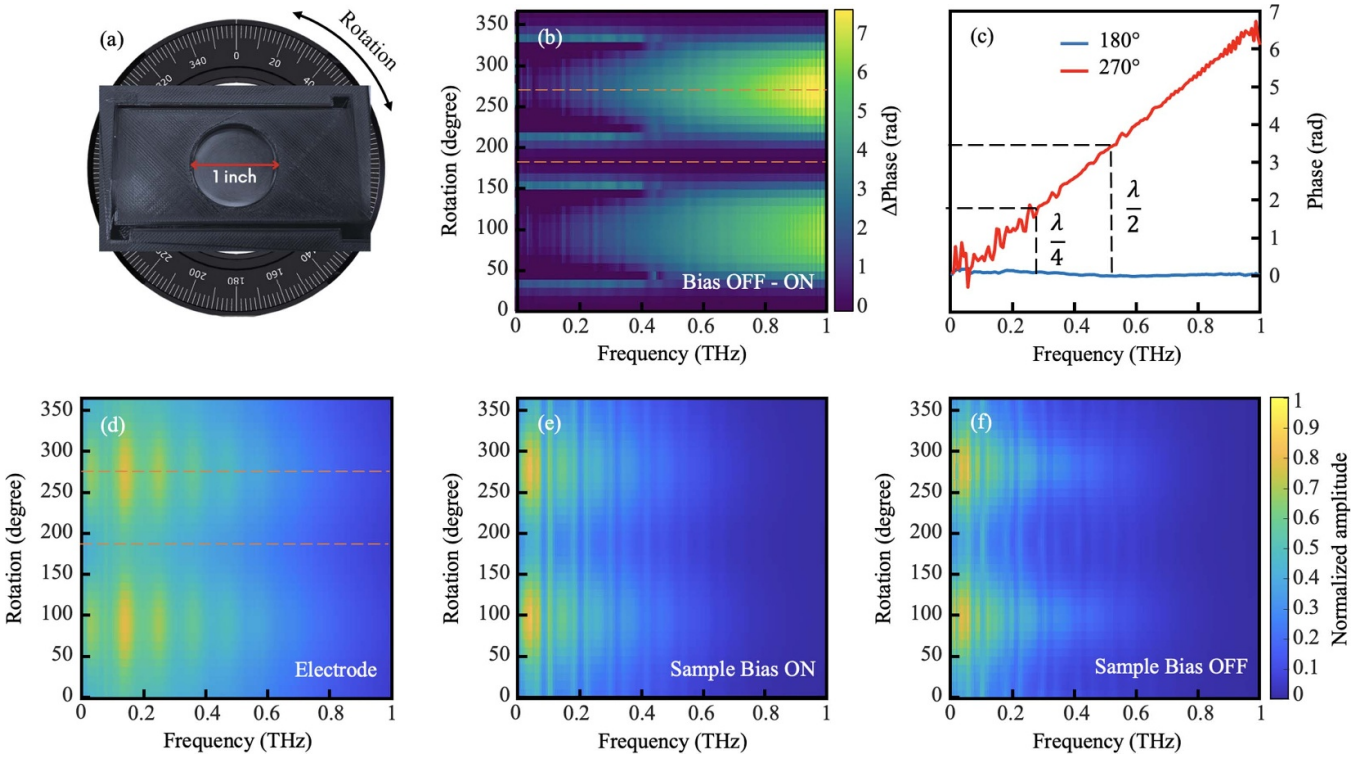

Figure 3. (a) Visible image of the LC sample with its rotating mount. (b) Phase shift vs. frequency at various angles, with (c) showing maximum (red) and minimum (blue) phase shifts. (d) Normalized transmission of a single glass substrate with ITO electrode. Normalized transmission of the LC sample (e) without bias voltage, and (f) with bias voltage. All data are normalized to a reference pulse in air without sample, and taken as a function of THz bandwidth and sample rotation angle.

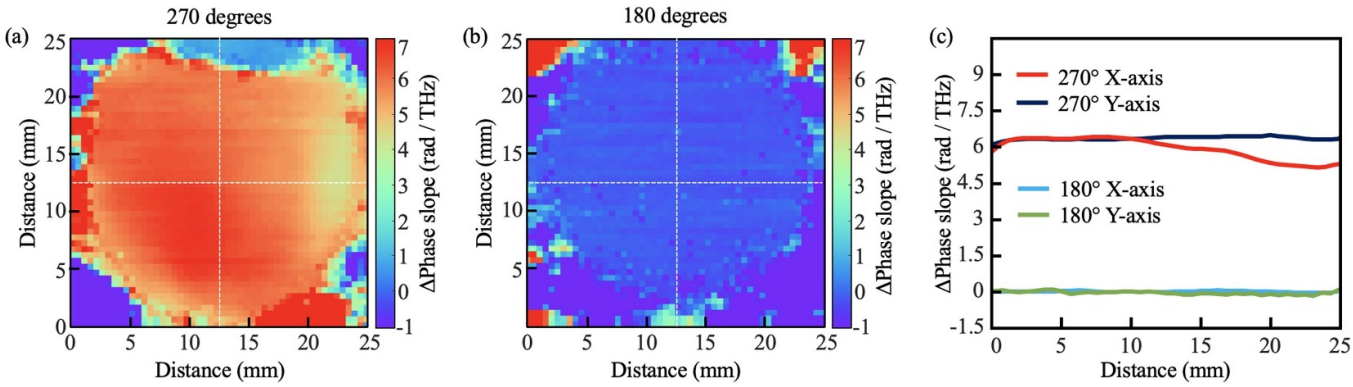

Figure 4. (a) TDS image of phase shift between non-active and active cell at 180 degrees. (b) TDS image of phase shift between non-active and active cell at 270 degrees. (c) Phase shift between non-active and active vs position on the cell at different angle.

these two cases are shown in figure 3(c). This figure demonstrates a significant phase shift occurring within the frequency range of 100 GHz to 1 THz. Specifically, the LC device functions as a quarter-wave plate (1.57 radians) at 260 GHz and as a half-wave plate (3.14 radians) at 520 GHz. However, based on the value of Δn reported in [24] and using equation (2), the maximum phase shift for mixture 1825 in a 1.6 mm thick cell is estimated to be 6.4 radians at 500 GHz. The smaller phase shift observed in this study is likely due to imperfect alignment of the LC in the thick cell and a possible overestimation of the actual thickness of the LC material. Additionally, according to previous work [24], mixture 1825 is expected to exhibit an extraordinary index of 1.948 at 500 GHz, which is higher than the value of 1.76 measured in this study at 300 GHz with the sample oriented at 270 degrees. In fact, the cell's visually milky appearance suggests non-ideal alignment of the LC, and figure 4 below will further illustrate the nonuniform thickness of the LC material, which could explain this discrepancy.

Next, we measured the normalized amplitude transmission across the frequency range of 0–1 THz for different rotation angles in three specific cases: (d) a glass plate with an ITO interdigital electrode, (e) biased LC device, and (f) unbiased LC device. All normalized transmissions are obtained from

the FFT response of the sample compared with the FFT of a pulse propagating only in air (without sample). In figure 3(d), the modulation of the normalized transmission as a function of the rotation angle of the single substrate with the ITO electrode layer is influenced solely by the attenuation of the electric field parallel to the electrode stripes. This attenuation is similar to the effect produced by a wire grid polarizer on an electromagnetic wave [29]. It is important to note that the strongest transmission is observed at 270 degrees and 90 degrees, where phase changes are maximal. In these normalized transmission data, an additional oscillation is observed as a function of frequency. As mentioned previously, this behavior results from the echo of the glass substrate in the time domain, which converts into oscillations in the frequency domain. A second important result in figures 3(e) and (f) is that the normalized amplitude transmission remains virtually unchanged with and without V-bias. Unfortunately, above 1 THz, high absorption losses make it extremely difficult to develop THz LC cells using glass substrate that can operate efficiently at these frequencies. To overcome this problem, a new substrate with a lower absorption coefficient (such as diamond) could be used. The second important piece of information is to note that maximum absorption occurs for rotation angles that will not be used when activating the cell polarization field (e.g. for angles around 0° or 180°).

3.2. Active phase modulation

To assess the impact of angle of rotation and applied V-bias on LCs, we recorded both amplitude and phase of the signal at different frequencies from 0 to 1 THz. Phase information was extracted from the angle value after performing a Fourier transform (FFT) on the time-domain data. The phase spectrum, derived directly from the angle between the real and imaginary parts of the transfer function, is generally bounded between $-\pi$ and π. This wrapping phenomenon means that whenever the phase value exceeds π in absolute magnitude, it wraps around the opposite polarity of 2π. This effect, known as phase wrapping, also occurs when performing FFT on noisy signals. It is therefore vital to differentiate between a legitimate phase jump, i.e. one that arises from a significant phase change, and a phase jump related to the low signal-to-noise ratio of the data, which therefore does not correspond to a real phase change. To mitigate this bias, a modified Blackman Window is applied to each time-domain data before proceeding with the FFT calculation, i.e. attenuating the values at both ends using cosines:

$$\begin{cases} w(i) = 0.5\left(\cos\left(\frac{\pi}{a_s - 1}\left(i - (a_s - 1)\right)\right) + 1\right), 0 \le a_s & (6) \\ w(i) = 1, a_s \le i \le n - a_e & (7) \\ w(i) = 0.5\left(\cos\left(\frac{\pi}{a_e - 1}\left(i - (n - a_e)\right)\right) + 1\right) & (8) \end{cases}$$

a_s represents the length of the region at the start, a_e the length of the region at the end, and n, the total length of the pulse.

Although this filtering procedure reduces the occurrence of phase wrapping in a single time-domain trace, extracting the phase angle from a time-domain hypercube (a 2D spatial mapping of a sample with the third dimension being temporal evolution) may still result in 2π phase jumps across all three axes. To ensure a continuous phase distribution along both spatial and spectral axes, a 3D phase unwrapping algorithm is employed to unwrap the phase information in 2D [31]. This algorithm has been selected due to its low time complexity allowing it to function seamlessly on large images. The linear relationship between the frequency and the unwrapped phase allows the reconstruction of an image by using the slope of the linear regression in every pixel. The region is determined by finding the start and stop indices that maximize the coefficient of determination ($R2$) of the linear fit on regions of varying length. To reduce time complexity, this operation is only performed on the pixel located at the center of the images.

Using this algorithm, figures 4(a) and (b) represent the unwrapped differential phase of the full aperture, when bias is on and then off, of THz data measured for two distinct angles where maximum and minimum phase shifts occurred: 180° and 270°, respectively. In figure 4(a), the maximum phase shift as a function of frequency, in units of (rad THz^{-1}), can be directly extracted from the above algorithm, with a linear fit. It can also be seen that a rotation difference of 90° from the maximum position at 270° results in a minimal phase shift, as shown in figure 4(b). Indeed, a near-zero differential phase shift is observed at the 180° rotation position, as expected based on the LC orientation shown in figure 3(b).

In these differential raster-scan imaging in transmission mode, a quick assertion of the LC device can be made. The red and blue tones indicate the areas with the highest and lowest phase differences, respectively. To understand this linear behavior of the differential phase change as a function of THz frequency, figure 3(c) illustrates this dependence for the two orientations of 180° and 270°. However, as seen in figure 4(a), certain areas, such as the right-side part of the sample at 270°, reveal a smaller phase difference which may be the consequence of a thinner layer of LC (cell deformation during the manual fabrication). To visualize the variation in the differential phase distribution, figure 4(c) displays the rad THz^{-1} profile extracted for the two rotation cases. These curves were obtained along the X and Y directions from the white dotted lines VIS in figures 4(a) and (b). The difference between the cross-sections of the X and Y axes clearly indicates the spatial inhomogeneity within the cell. In fact, the phase decrease beyond 20 mm observed at 270° along the x-axis in figure 4(c) is due to LC inhomogeneity. The phase difference is linearly proportional to the LC thickness, so a thinner LC layer results in a smaller phase difference, as shown in figure 4(c). Over time, when the device is stored vertically, the LC molecules shift within the cell, causing uneven distribution and disrupting uniform alignment. This variation in refractive index leads to inconsistent phase transmission and the decrease observed in the measurements.

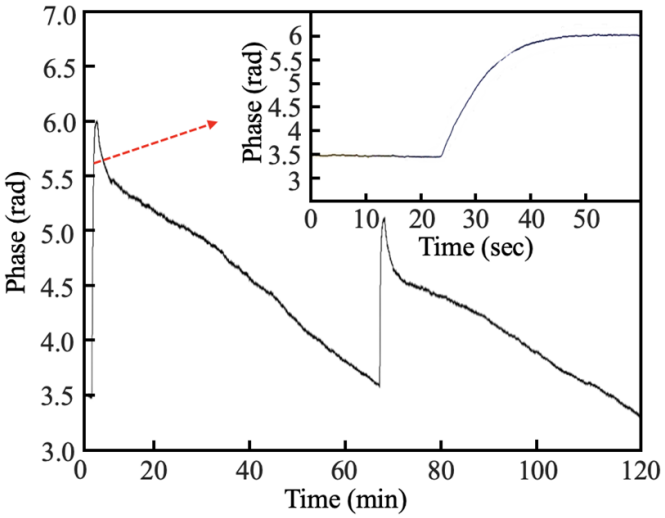

Figure 5. Real-time phase response to voltage activation and deactivation. Zoomed view of activation in inset.

3.3. Relaxation time measurement of the LC molecules

The response times are crucial for investigating any active modulator. For a 1.6 mm thick LC solution, we expect that the turn-on (τ_{on}) and turn-off (τ_{off}) times will be relatively long, as indicated by the following equations [31]:

$$\tau_{off} = \frac{\gamma_1 d^2}{K_x \pi^2} \tag{9}$$

$$\tau_{on} = \frac{\tau_{off}}{\left|\left(\frac{V}{V_{th}}\right)^2 - 1\right|} \tag{10}$$

$$V_{th} = \sqrt{\frac{K_x}{\varepsilon_0 \Delta\varepsilon}} \tag{11}$$

where $\Delta\varepsilon$ and V are the dielectric anisotropy of the LC and the switching V-bias of the cell respectively, γ_1 is the rotational viscosity and K_x is the appropriate expression for the elastic constant of the LC mixture, which is dependent upon the alignment of the LC cell. V_{th} is the threshold voltage of the LC cell.

Given the squared dependence of activation and deactivation times on thickness, fast devices at THz frequencies require thin cells filled by materials with relatively high birefringence [14]. While the birefringence of LC mixtures is well documented at VIS frequencies, their properties at THz frequencies are less well understood. Figure 5 shows phase changes in real time relative to the off state (no voltage on the electrodes) at 0.3 THz, with the inset showing a close-up view of the phase change relative to the on state (presence of a polarized voltage). This measurement was performed using a continuous-wave (CW) THz system, as described previously [32]. This result demonstrates that phase modulation at frequencies below 500 GHz is feasible using mixture 1825 with an LC thickness of 1.6 mm, whereas such modulation was previously limited to 500 GHz [24].

As it is also observed in figure 5, the molecules respond rapidly to the electric field once the voltage is applied, but natural relaxation is slower. Our measurements indicate a switching time of 16 s for the device. It should be noted that the response is fast under an electric field due to $\tau_{on} \propto 1/E^2$ thanks to our large applied DC field of 12.5 V m^{-1} . However, complete relaxation of the molecules in the LC to their initial planar position takes around an hour, indicating a significant delay once the electric field is removed, as $\tau_{off} \propto d^2$. Fortunately, this long response time could be improved by introducing an additional set of electrodes to return the molecules to their initial state [33]. We are currently testing next generation of electrodes (patent pending), which would allow not only generating an electric field that is perpendicular to cell substrates (used to reorient molecules from their ground state), but also, when desired, we can generate electrical field with a significant component that is parallel to these substrates. This should allow helping bringing back the molecular orientation much faster than the natural relaxation. We shall report the corresponding results soon.

4. Conclusion

In summary, we have fabricated and fully characterized a large aperture LC cells using THz time domain spectroscopy and raster scanning imaging. We found that the LC cells operate in the low THz frequency range, specifically between 100 GHz and 1 THz. Additionally, we demonstrated that the maximum relative phase difference corresponds to the maximum transmission of the LC cell, which is crucial for future applications. Moreover, THz-TDS coupled with raster imaging capability proved sufficiently sensitive for studying these cells and mapping the inhomogeneity of LC thickness across the entire aperture. We also determined that our large aperture LC cell functions as a controllable quarter-wave plate and half-wave plate at 0.26 THz and 0.52 THz, respectively. In summary, our work confirms the fabrication process for aligning molecules in a 1.6 mm thick LC cell. We also validate the functionality of our novel ITO electrode configuration for THz waves. THz-TDS successfully characterized the 2D mapping of phase changes, and real-time CW THz phase tracking monitored the LC sample's switching time. This study paves the way for future characterization of LC cells operating at THz frequencies, essential for enabling applications such as THz modulators.

Data availability statement

All data that support the findings of this study are included within the article (and any supplementary files).

Acknowledgment

Funding. F B gratefully acknowledges financial support from NSERC Grant Number 2023-03322, and the CRC tier2 Grant Number CRC-2019-127 on Spatiotemporal encryption of THz light. T G thanks NSERC for the grant 05888, CRC for the Grant 230212 and the Volkswagen Group Innovation for their valuable advises.

Conflicts of interests

The authors declare no conflicts of interests.

ORCID iDs

A Le Bourlout https://orcid.org/0009-0008-9429-2855
J Lafrenière-Greig https://orcid.org/0009-0007-8316-8683
F Blanchard https://orcid.org/0000-0002-3335-7458

References

[1] Ma Z T, Geng Z X, Fan Z Y, Liu J and Chen H D 2019 Modulators for terahertz communication: the current state of the art *Research* 2019 6482975
[2] Guerboukha H, Nallappan K and Skorobogatiy M 2018 Toward real-time terahertz imaging *Adv. Opt. Photon.* **10** 843
[3] Yurduseven O, Assimonis S D and Matthaiou M 2020 Intelligent reflecting surfaces with spatial modulation: An electromagnetic perspective *IEEE Open J. Commun. Soc.* **1** 1256–66
[4] Ahmad R, Ropagnol X, Trinh N D, Bois C and Blanchard F 2024 Reconfigurable screen-printed terahertz frequency selective surface based on metallic checkerboard pattern *Flex. Print. Electron.* **9** 025005
[5] Yang Y, Forbes A and Cao L 2023 A review of liquid crystal spatial light modulators: devices and applications *Opt.—Electron. Sci.* **2** 230026–1
[6] Lin Y-H, Wang Y-J and Reshetnyak V 2017 Liquid crystal lenses with tunable focal length *Liq. Cryst. Rev.* **5** 111–43
[7] Galstian T, Sova O, Asatryan K, Presniakov V, Zohrabyan A and Evensen M 2017 Optical camera with liquid crystal autofocus lens *Opt. Express* **25** 29945–64
[8] Ding C, Meng F-Y, Mu H-L, Lv J-F, Liu Y-H, Fang Q-Y, Xu S-S and Wu Q 2019 Bifunctional co-design of liquid crystal phase shifter and band-stop filter *J. Phys. D: Appl. Phys.* **52** 415002
[9] Wu J *et al* 2020 Liquid crystal programmable metasurface for terahertz beam steering *Appl. Phys. Lett.* **116** 131104
[10] Sahoo A K, Lin Y-H, Yang C-S, Wada O, Yen C-L and Pan C-L 2022 Electrically tunable dual-layer twisted nematic liquid crystal THz phase shifters with intermediate composite polymer thin film *Opt. Mater. Express* **12** 4733
[11] Wang J, Tian H, Li S, Wang G, Wang Y, Li L and Zhou Z 2020 Dual-band terahertz switch with stretchable bloch-mode metasurface *New J. Phys.* **22** 113008
[12] Deng G, Hu H, Mo H, Yin Z, Lu H, Hu M, Li J and Yang J 2022 Liquid crystal-based wide-angle metasurface absorber with large frequency tunability and low voltage *Opt. Express* **30** 22550
[13] Nickpay M-R, Danaie M and Shahzadi A 2022 Highly sensitive THz refractive index sensor based on folded split-ring metamaterial graphene resonators *Plasmonics* **17** 237–48
[14] Neuder R, Späth M, Schüßler M and Jiménez-Saez A 2024 Architecture for sub-100 ms liquid crystal reconfigurable intelligent surface based on defected delay lines *Commun. Eng.* **3** 70
[15] Kowerdziej R, Olifierczuk M, Parka J and Wróbel J 2014 Terahertz characterization of tunable metamaterial based on electrically controlled nematic liquid crystal *Appl. Phys. Lett.* **105** 022908
[16] Chen C-C, Chiang W-F, Tsai M-C, Jiang S-A, Chang T-H, Wang S-H and Huang C-Y 2015 Continuously tunable and fast-response terahertz metamaterials using in-plane-switching dual-frequency liquid crystal cells *Opt. Lett.* **40** 2021
[17] Shen Z, Zhou S, Ge S, Duan W, Chen P, Wang L, Hu W and Lu Y 2018 Liquid-crystal-integrated metadevice: towards active multifunctional terahertz wave manipulations *Opt. Lett.* **43** 4695
[18] De Gennes P G and Prost J 1993 *The Physics of Liquid Crystals* No. 83 (Oxford University Press)
[19] Degl'Innocenti R, Lin H and Navarro-Cia M 2022 Recent progress in terahertz metamaterial modulators *Nanophotonics* **11** 1485–514
[20] Chen C-Y, Hsieh C-F, Lin Y-F, Pan R-P and Pan C-L 2004 Magnetically tunable room-temperature 2 pi liquid crystal terahertz phase shifter *Opt. Express* **12** 2625–30
[21] Wu H, Hsieh C-F, Tang T-T, Pan R-P and Pan C-L 2006 Electrically tunable room-temperature 2π liquid crystal terahertz phase shifter *IEEE Photonics Technol. Lett.* **18** 1488–90
[22] Yang C S, Kuo C, Tang C C, Chen J C, Pan R P and Pan C L 2015 Liquid-crystal terahertz quarter-wave plate using chemical-vapor-deposited graphene electrodes *IEEE Photon. J.* **7** 1–8
[23] Ji Y, Fan F, Zhang Z, Cheng J and Chang S 2022 Active terahertz liquid crystal device with carbon nanotube film as both alignment layer and transparent electrodes *Carbon* **190** 376–83
[24] Reuter M, Vieweg N, Fischer B M, Mikulicz M, Koch M, Garbat K and Dąbrowski R 2013 Highly birefringent, low-loss liquid crystals for terahertz applications *APL Mater.* **1** 012107
[25] Petrov N V, Sokolenko B, Kulya M S, Gorodetsky A and Chernykh A V 2022 Design of broadband terahertz vector and vortex beams: I. Review of materials and components *Light Adv.Manuf.* **3** 640–52
[26] Neu J and Schmuttenmaer C A 2018 Tutorial: an introduction to terahertz time domain spectroscopy (THz-TDS) *J. Appl. Phys.* **124** 231101
[27] Chodorow U, Parka J, Kula P, Herman J, Chojnowska O, Dabrowski R and Chigrinov V G 2013 Terahertz properties of fluorinated liquid crystals *Liq. Cryst.* **40** 1586–90
[28] Pusenkova A , Meinecke M-M , Kurz H G , Gisder T , Schroeder H and Galstian T 2024 Liquid crystal dynamically steerable GHz and THz devices for automotive and other applications *2024 Int. Radar Symp. (IRS) (Wroclaw, Poland, 2024)* pp 66–69
[29] Mansourian M, Zhuldybina M, Ropagnol X, Trinh N D, Bois C and Blanchard F 2021 Fabrication and characterization of a terahertz polarizer from a roll-to-roll printer *2021 Photonics North (PN)* (IEEE) pp 1–1
[30] Blanchard F, Sumida K, Wolpert C, Trotsalas M, Tanaka T, Doi A, Kitagawa S, Cooke D G, Furukawa S and Tanaka K 2014 Terahertz phase contrast imaging of sorption kinetics in porous coordination polymer nanocrystals using differential optical resonator *Opt. Express* **22** 11061–9
[31] Herráez M A, Burton D R, Lalor M J and Gdeisat M A 2002 Fast two-dimensional phase-unwrapping algorithm based on sorting by reliability following a noncontinuous pat *Appl. Opt.* **41** 7437–44
[32] Le Bourlout A, Pusenkova A, Zhuldybina M, Ropagnol X, Galstian T and Blanchard F 2023 Characterization of active liquid crystal with continuous terahertz waves *2023 Photonics North (PN)* (IEEE) pp 1–2
[33] Oh-e M and Zheng D Y 2023 Reversibly switching liquid crystals between three orthogonal orientation states for use in rapid-response THz phase shifters *Opt. Express* **31** 8632–40